

Effect of particle shape on packing fraction and velocity profiles at outlet of a silo

Qing-Qing Gao(高庆庆), Yu-Chao Chen(陈玉超), and Lin Hu(胡林)

Citation: Chin. Phys. B, 2023, 32 (**6**): 064702. DOI: 10.1088/1674-1056/aca204
Journal homepage: http://cpb.iphy.ac.cn; http://iopscience.iop.org/cpb

What follows is a list of articles you may be interested in

Flow and clogging in a horizontal silo with a rotary obstacle

Cong-Cong Xu(徐聪聪), Qing-Fan Shi(史庆藩), Wei Liu(刘伟), and Ning Zheng(郑宁)
Chin. Phys. B, 2023, 32 (**4**): 044701. DOI: 10.1088/1674-1056/ac7a19

Mechanism from particle compaction to fluidization of liquid-solid two-phase flow

Yue Zhang(张悦), Jinchun Song(宋锦春), Lianxi Ma(马连喜), Liancun Zheng(郑连存), Minghe Liu(刘明贺)
Chin. Phys. B, 2020, 29 (**1**): 014702. DOI: 10.1088/1674-1056/ab5789

Numerical simulations of dense granular flow in a two-dimensional channel:The role of exit position

Tingwei Wang(王廷伟), Xin Li(李鑫), Qianqian Wu(武倩倩), Tengfei Jiao(矫滕菲), Xingyi Liu(刘行易), Min Sun(孙敏), Fenglan Hu(胡凤兰), Decai Huang(黄德财)
Chin. Phys. B, 2018, 27 (**12**): 124704. DOI: 10.1088/1674-1056/27/12/124704

Gas flow characteristics of argon inductively coupled plasma and advections of plasma species under incompressible and compressible flows

Shu-Xia Zhao(赵书霞), Zhao Feng(丰嬰)
Chin. Phys. B, 2018, 27 (**12**): 124701. DOI: 10.1088/1674-1056/27/12/124701

A fractal approach to low velocity non-Darcy flow in a low permeability porous medium

Cai Jian-Chao (蔡建超)
Chin. Phys. B, 2014, 23 (**4**): 044701. DOI: 10.1088/1674-1056/23/4/044701

Effect of particle shape on packing fraction and velocity profiles at outlet of a silo

Qing-Qing Gao(高庆庆)[1], Yu-Chao Chen(陈玉超)[2], and Lin Hu(胡林)[1,†]

[1] *College of Physics, Guizhou University, Guiyang* 550025, *China*
[2] *Department of Civil Engineering, Nanyang Normal University, Nanyang* 473061, *China*

(Received 1 September 2022; revised manuscript received 1 November 2022; accepted manuscript online 11 November 2022)

Many studies on how the particle shape affects the discharge flow mainly focus on discharge rates and avalanche statistics. In this study, the effect of the particle shape on the packing fraction and velocities of particles in the silo discharge flow are investigated by using the discrete element method. The time-averaged packing fraction and velocity profiles through the aperture are systematically measured for superelliptical particles with different blockinesses. Increasing the particle blockiness is found to increase resistance to flow and reduce the flow rate. At an identical outlet size, larger particle blockiness leads to lower velocity and packing fraction at the outlet. The packing fraction profiles display evidently the self-similar feature that can be appropriately adjusted by fractional power law. The velocity profiles for particles with different shapes obey a uniform self-similar law that is in accord with previous experimental results, which is compatible with the hypothesis of free fall arch. To further investigate the origin of flow behaviors, the packing fraction and velocity field in the region above the orifice are computed. Based on these observations, the flow rate of superelliptical particles is calculated and in agreement with the simulated data.

Keywords: superelliptical particles, flow rate, packing fraction and velocity profiles, discrete element method

PACS: 47.57.Gc, 83.10.Rs, 45.50.–j **DOI:** 10.1088/1674-1056/aca204

1. Introduction

Granular flow exists ubiquitously in nature and technological process. A huge number of experimental, analytical, as well as numerical studies, have been devoted over many years to gaining a deep understanding of the underlying process of granular flow.[1–5] Considering the complex dynamic behavior of the interaction between particles, the discrete element method (DEM) has proven to be practical and effective in understanding the macroscopic and microscopic properties of granular materials.[6–8] Predicting the discharge rate is important in designing of reliable and controllable transport systems but is difficult due to complexities associated with granular flow such as inhomogeneous solid distribution, irregular velocity profile, and diverse particle sizes and shapes.[9]

Based on dimensional analysis, Beverloo *et al.*[10] suggested that the discharge rate from a silo has the following law

$$Q = C\rho_{\rm b}\sqrt{g}\,(D-kd)^{n_{\rm S}+1/2}, \tag{1}$$

where $n_{\rm S}$ is the spatial dimension, and $n_{\rm S}=1$ and 2 for two- and three-dimensional (2D and 3D) space. D and d are the diameter of the outlet of the silo and the particle diameter, g is the acceleration of gravity. $\rho_{\rm b}$ is the bulk density of the material and C is a constant related to material properties. The term with k can be explained in the form of a shear zone adjacent to the edge of the orifice, where there are fewer particles. The power scaling law between mass flow rate and the opening size has been substantiated in previous studies.[11–17] A simple explanation of the Beverloo's equation is based on the concept of a "free-fall arch". In this scenario the arch is a surface spanning the exit at a height approximately D away from the exit. Above the surface, the particles behave like a solid and interact with each other. Below this surface, the particles are not in rigid contact and undergo a free fall with acceleration g. To understand the physical mechanism that governs the flow of particles through orifices, Janda *et al.*[18] conducted an experiment on the flow of granular medium from a 2D silo, and they showed that the velocity profiles and packing fraction profiles at the outlet are self-similar, and the rescaled velocity and density can be well fitted by $v(x)=v_{\rm c}\sqrt{[1-(x/R)^2]}$ and $\phi(x)=\phi_{\rm c}(1-(x/R)^2)^{0.33}$, where $v_{\rm c}(\phi_{\rm c})$ and x represent the value of velocity (packing fraction) in the outlet center and the horizontal position, and R is the radius of outlet ($R=D/2$). The scaling of the central velocity ($v_{\rm c}$) is related to the concept of a hypothetical free fall arch scaling with outlet size. Rubio-Largo *et al.*[19] revised the free fall arch postulate and explained the scaling of velocity at the exit with outlet size based on the scaling of acceleration profile. The scaling explains why the free-fall arch idea can serve as an approximation to describe the flow rate of hopper discharge. In reality, most of particle shapes are usually not spherical, therefore it is scientifically and industrially important to study how particle shape affects flow rheology and clogging mechanism. Several studies[20–34] have been performed to understand the effect of particle shape on the discharge flow through simula-

†Corresponding author. E-mail: hulin2018@sina.com

© 2023 Chinese Physical Society and IOP Publishing Ltd

tion by using DEM. Li *et al.*[22] and Langston *et al.*[23] found that elliptical particles discharge faster than the circular ones, which was explained by particle alignment yielding a lower resistance to flow. But later on, Liu *et al.*[25] showed that ellipsoidal particles with higher aspect ratio have a smaller flow rate on the basis of DEM simulation and experiment, and proposed a modified Beverloo' equation to describe the flow rate of ellipsoidal particles.

Despite the researches related to this issue, there is still a lack of physical understanding of how the shape of particle affects flow in a silo, in particular, the influences of particle shape on the density and velocity profiles of pouring particles at the outlet, which jointly govern the flow rate.

In this work, the steady-state granular flow in a 2D silo with a flat bottom is investigated by the DEM. Superelliptical particles with different blockinesses are used in the simulation. Firstly, the applicability of Beverloo's law to the flow rate of superelliptical particles is examined, then we systematically measure the packing fraction and velocity profile at the outlet and discuss how the particle shape affects those observations. The packing fraction and velocity field are also computed by coarse-graining method to explore the underlying flow characteristics. Finally, the mass flow rate of superelliptical particles is calculated based on these observations.

2. Simulation model and methods

2.1. Representation of particle shapes

The superquadric equation is effective in describing particle shapes. It was reported that the superquadric equation can be used to represent about 80% of the shapes of solids in nature.[7] The superquadric equation in 2D space is $|x/a|^m + |y/b|^n = 1$, where a and b are the semi-axis lengths of the superquadric elements in the x and y axes, m and n are the blockiness and determine the sharpness of the shape. In this work, we mainly focus on shapes with blockiness ($m = n$) that changes from 2 to 12, and take $a = b$.

2.2. Contact detection

An efficient and stable method is crucial to determining contact point between superellipes. The traditional Newton–Raphson method is usually used to find the contact point. However, to ensure the stability and efficiency of the superquadric DEM model, the values of blockiness are taken in the range of $1.4 < m$ and $n < 7$.[35] In this work, the contact points between superelliptical particles are determined by using the grid method[36–38] with no restriction on m and n. A brief description of the method is given below.

In the body-fixed coordinate system, consider two particles (denoted as i and j) with shape functions

$$f_i(\boldsymbol{x}) = \left|\frac{x}{a_i}\right|^{m_i} + \left|\frac{x}{b_i}\right|^{n_i} = 1, \tag{2}$$

$$f_j(\boldsymbol{x}) = \left|\frac{x}{a_j}\right|^{m_j} + \left|\frac{x}{b_j}\right|^{n_j} = 1. \tag{3}$$

The space-fixed coordinates can be transformed into the body-fixed ones by the following expressions:

$$\boldsymbol{x}' = R_i(\boldsymbol{X} - \boldsymbol{X}_i), \tag{4}$$

$$\boldsymbol{x}'' = R_j(\boldsymbol{X} - \boldsymbol{X}_j), \tag{5}$$

where R_i, R_j, $\boldsymbol{X}_i$, and $\boldsymbol{X}_j$ are the rotation matrices and the centroid of particles in the space-fixed coordinate system. The inverse transformation is

$$\boldsymbol{X} = R_i^{\mathrm{T}}\boldsymbol{x}' + \boldsymbol{X}_i, \tag{6}$$

$$\boldsymbol{X} = R_j^{\mathrm{T}}\boldsymbol{x}'' + \boldsymbol{X}_j, \tag{7}$$

with R_i^{T} and R_j^{T} being the transpose of R_i and R_j respectively. In the space-fixed coordinate system, the shape functions of two particles are

$$f_i(R_i(\boldsymbol{X} - \boldsymbol{X}_i)) = 1, \tag{8}$$

$$f_j(R_j(\boldsymbol{X} - \boldsymbol{X}_j)) = 1. \tag{9}$$

The coordinates $(\boldsymbol{x}')$ of a point on particle i in its body-fixed coordinate system can be transformed into $\boldsymbol{x}'' = \left(R_i^{\mathrm{T}}\boldsymbol{x}' + \boldsymbol{X}_i - \boldsymbol{X}_j\right) = R_i^{\mathrm{T}}(\boldsymbol{x}' + R_i(\boldsymbol{X}_i - \boldsymbol{X}_j))$ in the space-fixed coordinate system of particle j. This point is then substituted into the shape function of particle j in its body-fixed coordinate system as follows:

$$f_j\left(R_j R_i^{\mathrm{T}}\left(\boldsymbol{x}' + R_i(\boldsymbol{X}_i - \boldsymbol{X}_j)\right)\right) = \eta\left(\boldsymbol{x}'\right). \tag{10}$$

In the body-fixed coordinate system of particle j, the centroid of particle i is $R_i(\boldsymbol{X}_j - \boldsymbol{X}_i)$ and the rotation matrix is $R_j R_i^{\mathrm{T}}$. The boundary of a particle i is divided into a number of grids, and an arbitrary point in each segment is chosen to calculate $\eta(\boldsymbol{x}')$. The minimum value of $\eta(\boldsymbol{x}')$ $(\eta_{\min})$ and the corresponding point $\boldsymbol{x}'_{\min}$ on the boundary of particle i can be obtained. The interaction between the two particles is determined according to the value of $\eta_{\min}$. Two particles are tangent, overlapped and separated from each other when $\eta_{\min} = 1$, $\eta_{\min} < 1$, and $\eta_{\min} > 1$, respectively. The number of grids depends on the required calculation accuracy, and a higher calculation accuracy requires a larger number of grids.

2.3. Contact force models and system description

The nonlinear contact force model for spherical particles was developed[6] and then extended to the calculation of the force between superelliptical particles.[7] The mathematical expressions of contact forces and torques, as well as the parameters used in the simulation, are listed in Tables 1 and 2.

Table 1. Force and torque between particles.

Property	Equation
Normal overlapping	δ_n
Tangential displacement vector	$\hat{\boldsymbol{\delta}}_t = \boldsymbol{\delta}_t/\lvert\boldsymbol{\delta}_t\rvert$
Tangential maximum displacement	$\delta_{t,\max} = (\mu_s(2-\nu))/(2(1-\nu))\delta_n$
Poisson's ratio	ν
Effective Young's modulus	$E^* = E/(2-2\upsilon^2)$
Effective mass	$m_{ij} = m_i m_j/(m_i+m_j)$
Effective radius	$R^* = R_i R_j/(R_i+R_j)$
Normal spring force	$\boldsymbol{f}_{cn} = 4/3E^*\sqrt{R^*}\delta_n^{3/2}\hat{n}$
Normal viscous force	$\boldsymbol{f}_{dn} = -c_n(8m_{ij}E^*\sqrt{R^*\delta_n})^{1/2}\boldsymbol{v}_{n,ij}$
Tangential spring force	$\boldsymbol{f}_{ct} = -\mu_s\lvert\boldsymbol{f}_{cn}\rvert(1-(1-\delta_t/\delta_{t,\max})^{3/2})\hat{\boldsymbol{\delta}}_t$
Tangential viscous force	$\boldsymbol{f}_{dt} = -c_t(6\mu_s m_{ij}\lvert\boldsymbol{f}_{cn}\rvert\sqrt{1-\delta_t/\delta_{t,\max}}/\delta_{t,\max})^{1/2}\boldsymbol{v}_{t,ij}$
Torque	$\boldsymbol{q}_i = \boldsymbol{r}_{ic}\times(\boldsymbol{f}_{ct}+\boldsymbol{f}_{dt})$
Tangential maximum displacement	$\delta_{t,\max} = \mu_s(2-\nu)/(2-2\nu)\delta_n$
Relative sliding velocity	$\boldsymbol{v}_{ij} = \boldsymbol{v}_i - \boldsymbol{v}_j + \boldsymbol{\omega}_i\times\boldsymbol{r}_{ic} - \boldsymbol{\omega}_j\times\boldsymbol{r}_{jc}$
Normal relative velocity	$\boldsymbol{v}_{n,ij} = (\boldsymbol{v}_{ij}\cdot\hat{n})\hat{n}$
Tangential relative velocity	$\boldsymbol{v}_{t,ij} = \boldsymbol{v}_{ij} - \boldsymbol{v}_{n,ij}$
Relative rolling velocity	$\boldsymbol{v}_r = -\frac{r_{icn}r_{jcn}}{r_{ijn}}\hat{\boldsymbol{n}}\times(\boldsymbol{\omega}_i-\boldsymbol{\omega}_j)$
Rolling force	$\begin{cases}\boldsymbol{f}_0^r = -k_r\boldsymbol{\xi}_r - \gamma_r\boldsymbol{v}_r \\ \boldsymbol{f}_r = \min(\mu_r f_n, \lvert\boldsymbol{f}_0^r\rvert)\,\boldsymbol{f}_0^r/\lvert\boldsymbol{f}_0^r\rvert\end{cases}$
Rolling torque	$\mathbf{q}^{\text{rolling}} = \frac{r_{icn}r_{jcn}}{r_{ijn}}\hat{\boldsymbol{n}}\times\boldsymbol{f}_r$

Table 2. Parameters of simulations.

Parameters	Value	SI-units
Length-unit	1	1 mm
Mass-unit	1	1 mg
Time-unit	1	1 ms
Particle density	2.5	2.5×10^3 kg/m^2
Particle dimeter	2	2 mm
Young's modulus	10^6	1 GPa
Friction coefficient	0.50	0.50
Poisson's ratio	0.25	0.25
Normal viscosity coefficient	0.4	0.4
Tangential viscosity coefficient	0.4	0.4
Rolling stiffness	10^6	10^6 N/m
Rolling viscosity	10^3	1.0 kg/s
Rolling friction coefficient	0.005	0.005
Integration time-step	5×10^{-4}	10^{-7} s

2.4. System description and statistical averages

The 2D silo is shown in Fig. 1(a), where the height and width of the rectangular channel are $H = 900$ mm and $W = 100$ mm. The walls of the silo have the same material properties as the particles'. The outlet is located in the center of the flat bottom and its length is D, which can be changed at will.

The superelliptical particles with equal minor and major axis $d_{\text{maj}} = 2$ mm are adopted in the simulation, and the shape of particles varies with the blockiness n that changes from 2 to 12. The granular system consists of 10000 particles, and the initial particle system is prepared by random deposition of particles in a closed silo to minimize the gravitational potential energy. After the preparation phase, a slot is opened situated at the bottom of the silo, and simulation is running in a given time step.

The instantaneous flow rate as a function of time is shown in Fig. 1(b). At the beginning, the discharge rate reaches rapidly a steady value and then the flow rate fluctuates around a value, which corresponds to the steady flow. Finally, the flow rate starts to drop continuously. During the steady discharge, the number of discharged particles with time is counted at each given interval (200 time-step). The instantaneous flow rate is measured as $\Delta N/\Delta t$, where ΔN is the number of particles discharged from the silo during Δt. The steady-state flow rate (Q) is obtained from the time average of the instantaneous flow rate during the steady state.

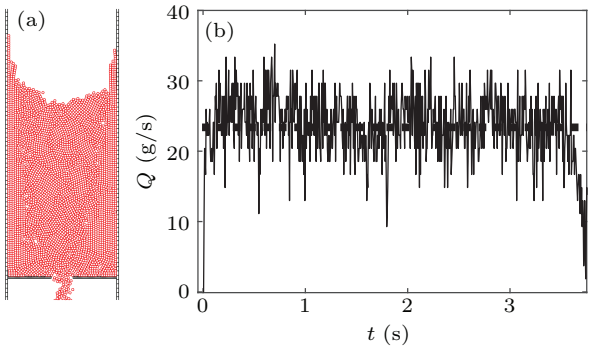


Fig. 1. (a) Snapshot of discharge flow from a silo. (b) Temporal evolution of instantaneous flow rate ($n = 6$, $D = 20$ mm), with dotted line representing the time-averaged flow rate.

We measure the packing fraction and velocity profiles of particles locally across the outlet. All particle velocities and positions are recorded in a snapshot every 500 time-step. The packing fraction and velocity are the average values of the set of the time-dependent snapshots of a steady granular flow.

Given that the flow is steady, this time average can be considered as an ensemble average according to the ergodicity. For each snapshot, the statistics are supposed to be homogeneous over a predefined rectangular domain. The width and height of this rectangle domain are $0.3d_{\mathrm{maj}}$ and d_{maj}, where d_{maj} ($= 2$ mm) is the major axis length of the particle, which is actually small compared with the spatial evolution of the profiles (that scales with D). We have checked that the choice of rectangular domain width has little effect on the results. In each snapshot, the vertical velocity of each particle within each rectangular domain can be obtained and the velocity profile at the outlet is obtained as the ensemble average of the entire snapshot sequences. The area of each particle inside a predefined domain is determined in each snapshot, and the packing fraction profiles is then obtained by averaging all snapshots. Given the profiles of packing fraction and velocity at the outlet, the flow rate of superelliptical particles can be predicted and compared with the simulation data. The coarse-graining technique[19,20] is implemented to obtain the steady flow map. We first coarsegrain the particle tracking data for each sequential snapshot, and then perform the time average.

2.5. DEM model verification

To verify the reliability of the DEM model, the contact models and parameters in Tables 1 and 2 are used to simulate the discharge flow of disks. The dependence of mass flow rate on outlet size can be fitted satisfactorily by Beverloo's law (Fig. 2(a)), and the value of fitting parameter k is compatible with those reported in previous work, where k is 1.85 (Ref. [16]) and 1.82 (Ref. [17]). Figure 2(b) presents the spatial vertical velocity field computed based on the simulated data, and the present simulated result is comparable to the experimental result,[19] which verifies that the current DEM model can be used to simulate the basic characteristics of granular flow.

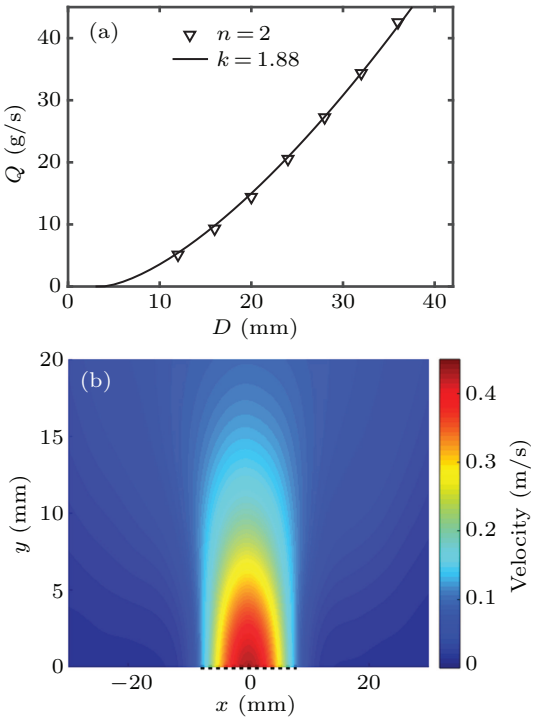


Fig. 2. (a) Mass flow rate as a function of outlet size for disks. Symbols represent simulated data, and the continuous line is the fitting by Eq. (1). (b) Vertical velocity field for disks ($D = 16$ mm), and the used Gaussian coarse-graining function is the same as that in Ref. [19]. The x indicates the distance to the center of the outlet, and the y is the height from the bottom of the silo. The dotted line indicates the orifice.

3. Results and discussion

3.1. Flow rate from simulation

We will first focus on the evolution of simulated flow rate with outlet size (Fig. 3). The disks have the highest flow rate because they are the most free-flowing. Departures from circularity result in a decrease of the flow rate. It should be noted that when $n = 8$ or greater, the variations in particle shape fail to make an obvious difference in the flow rate. As the blockiness increases, the jamming is more likely to occur, *i.e.*, for blockinesses $n = 6$, 8, 10, and 12, the steady flow can be sustained only when the outlet size is greater than or equal to $8d_{\mathrm{maj}}$, $10d_{\mathrm{maj}}$, $12d_{\mathrm{maj}}$, and $14d_{\mathrm{maj}}$, respectively. The increase of blockiness leads to the development of face-to-face contacts between faceted particles that can resist torque and enhance bridging, thereby increasing clogging capability.[24,33] The simulated flow rates for all cases can be fitted with Beverloo's equation, where d is chosen as the axis length of the particle. The parameter k corresponding to disk is compatible with that obtained in Refs. [16,17], and found to be dependent on the particle shape, as indicated in the literature.[39] To shed light on how the particle shape affects the flow properties of particles from a silo, the packing fraction and velocity profiles at the outlet are systematically measured and analyzed as discussed below.

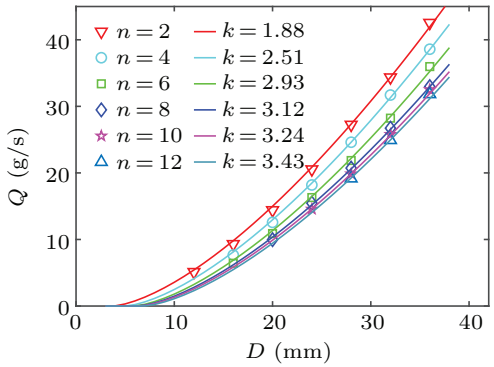


Fig. 3. Curves of mass flow rate *versus* outlet size for particles with various blockinesses. The symbols represent simulated results and the continuous lines correspond to the results from Beverloo's law.

3.2. Packing fraction and velocity profiles at outlet

One of factors governing the flow rate of particles is the packing fraction at the outlet. Figures 4(a)–4(f) show the time-averaged packing fraction profiles across the outlet for

particles with different blockinesses, in which the origin corresponds to the center of the outlet. It is shown that the value of packing fraction increases with outlet size for superelliptical particles. This is explicable because a strong dilatancy is required to avoid forming arches that can cause clogging in the case of small orifices. To verify the self-similarity of the profiles observed experimentally by Janda *et al.*,[18] we normalize the packing fraction by the central packing fraction at the outlet (ϕ_c) and rescale the horizontal position by R as shown in Figs. 4(a′)–4(f′). The data almost collapse into a single curve for all cases. The collapsed data can be fitted by

$$\phi(x) = \phi_c \left[1 - \left(\frac{x}{R}\right)^2\right]^{\nu_\phi}, \tag{11}$$

and the fitting parameters are $\nu_\phi = 0.19$, $\nu_\phi = 0.28$, $\nu_\phi = 0.32$, $\nu_\phi = 0.36$, $\nu_\phi = 0.40$, and $\nu_\phi = 0.43$, for particles with different blockinesses, say $n = 2$, $n = 4$, $n = 6$, $n = 8$, $n = 10$, and $n = 12$, respectively. The fitting parameters for disks are compatible with those reported in the literature.[18,40] The fitting parameter ν_ϕ that regulates the profile curvature shows increase with the blockiness, suggesting that the particle shape potentially affects the packing fraction's spatial distribution in the core flow region above the orifice.

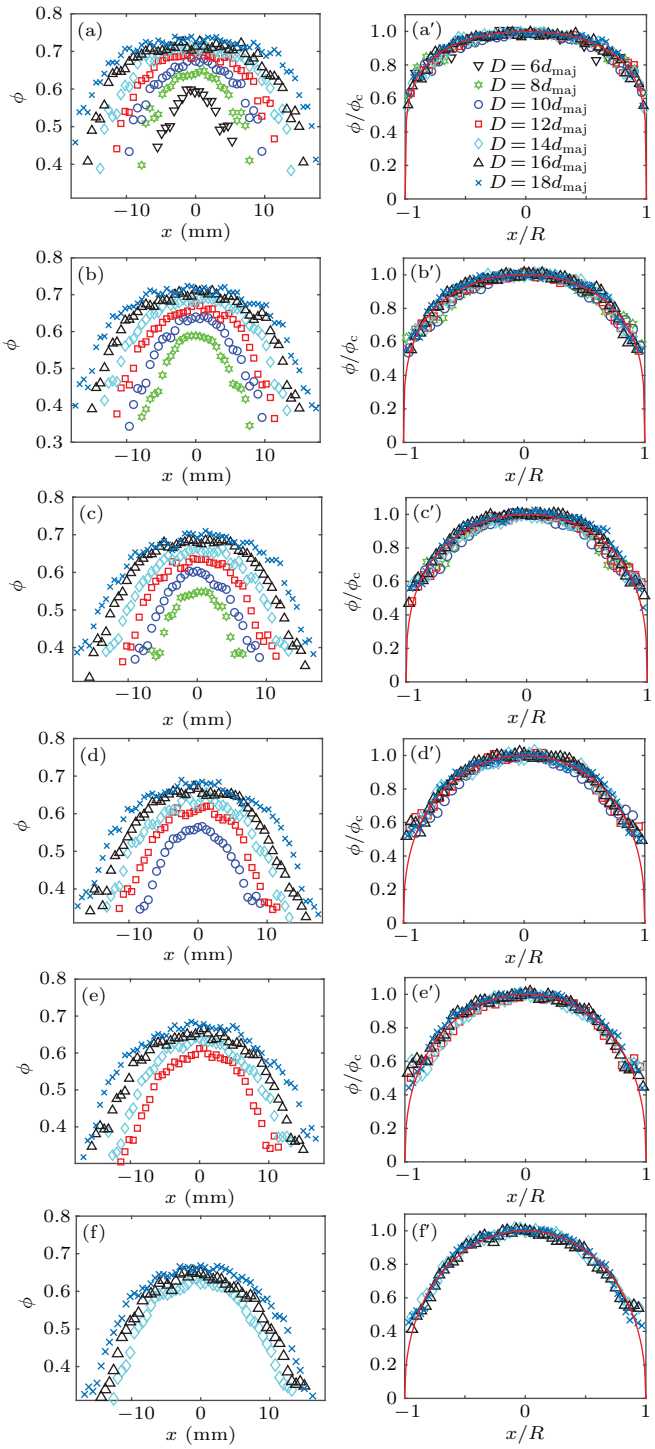


Fig. 4. Horizontal volume fraction profiles *versus* x for (a) disks and superelliptical particles with blockiness $n = 4$ (b), 6 (c), 8 (d), 10 (e), and 12 (f). (a′)–(f′) Normalized packing fraction *versus* position rescaled by R. The continuous line corresponds to Eq. (11), and symbols are in panel (a′).

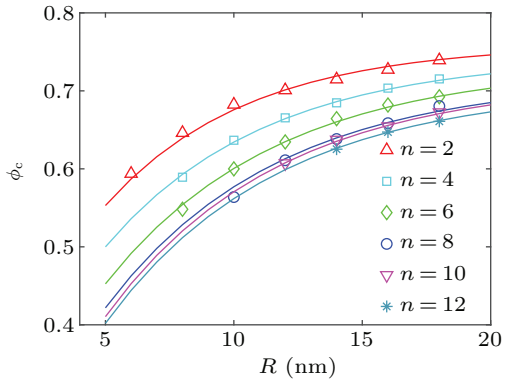


Fig. 5. Plots of packing fraction in the center of the outlet as a function of R for particles with different blockinesses (symbols). The continuous lines correspond to Eq. (12).

Now we turn to investigating the evolution of packing fraction at the outlet center shown in Fig. 5. At a certain outlet size, the value of ϕ_c increase with blockiness, but when $n = 8$ or larger, the effect of blockiness on ϕ_c becomes inconspicuous due to the very subtle variations in particle shape. For all systems, ϕ_c exhibits an asymptotic growth with outlet size, which can be suitably described by an exponential saturation as follows:

$$\phi_c = \phi_\infty \left[1 - \alpha \exp(-\beta R)\right]. \tag{12}$$

In the case of disks, the asymptotic value of ϕ_c for very big orifice $\phi_\infty = 0.76$, which is comparable to that in Ref. [16]. The other fitting parameters are $\alpha = 0.66$ and $\beta = 0.19$ mm^{-1}, which match the experimental results.[18] For superellipses, the fitting parameters are $\phi_\infty = 0.74$, $\alpha = 0.73$, and $\beta = 0.16$ mm^{-1} ($n = 4$); $\phi_\infty = 0.73$, $\alpha = 0.81$, and $\beta = 0.16$ mm^{-1} ($n = 6$); $\phi_\infty = 0.72$, $\alpha = 0.87$, and $\beta = 0.15$ mm^{-1} ($n = 8$); $\phi_\infty = 0.71$, $\alpha = 0.9$, and $\beta = 0.15$ mm^{-1} ($n = 10$); $\phi_\infty = 0.71$, $\alpha = 0.91$, and $\beta = 0.15$ mm^{-1} ($n = 12$). For comparisons, the bulk packing fraction is $\phi_b = 0.80$ (disks), $\phi_b = 0.81$ ($n = 4$), $\phi_b = 0.82$ ($n = 6$), $\phi_b = 0.82$ ($n = 8$), $\phi_b = 0.83$ ($n = 10$), and $\phi_b = 0.83$ ($n = 12$). Hence, $\phi_\infty < \phi_b$ for all systems, suggesting that the density of the granular media passing through

the outlet should be lower than the bulk density. As blockiness increases, the dependence of parameters α and β on blockiness tends to be very weak. In Eq. (12). The factor $\left[1-\alpha^{-\beta R}\right]$ characterizes the dilatancy under the geometrical constraint.[40]

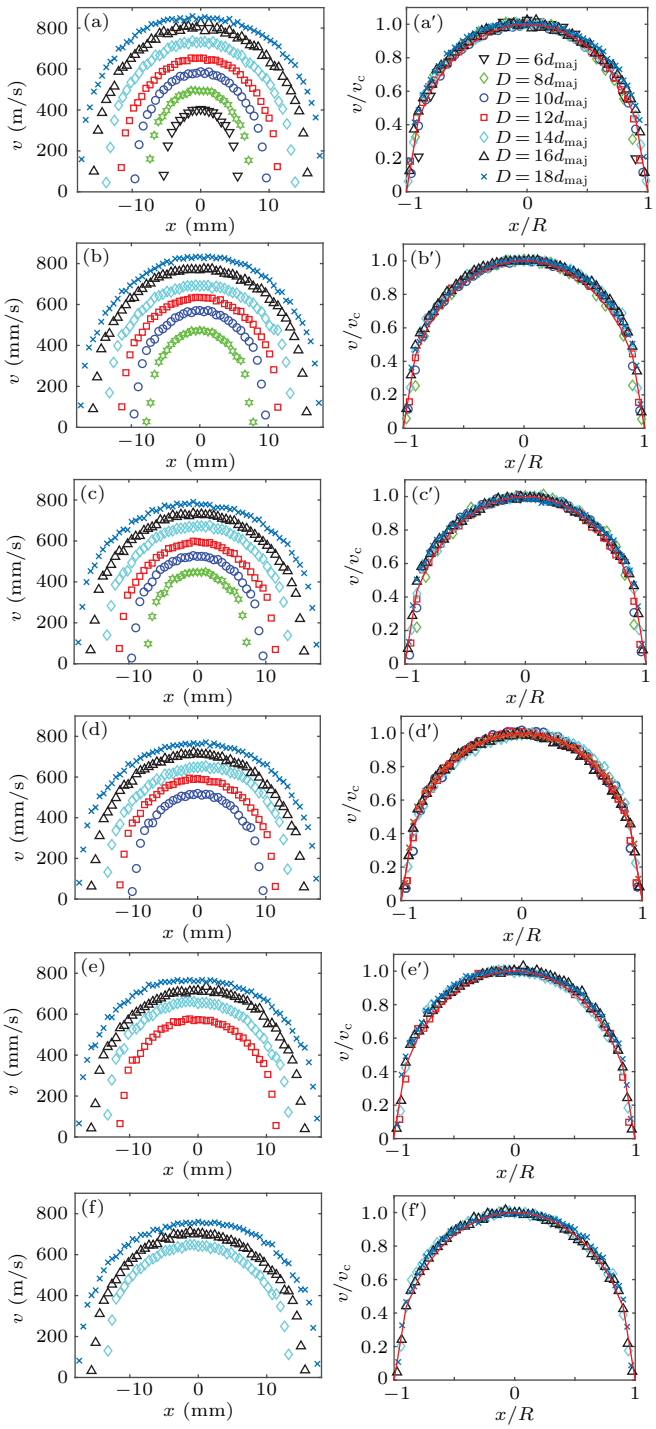


Fig. 6. Vertical velocity profiles for (a) disks and superelliptical particles with blockinesses $n = 4$ (b), 6 (c), 8 (d), 10 (e), and 12 (f). (a′)–(f′) Normalized velocities *versus* rescaled position (x/R). The continuous line corresponds to Eq. (13) and symbols are in panel (a′).

Another factor governing the flow rate is the particle's vertical velocity at the outlet. Figures 6(a)–6(f) present the time-averaged vertical velocity profiles at the outlet for particle systems with blockinesses ranging from 2 to 12. The vertical velocity of particles decreases as the outlet size decreases, and the profiles for various outlet sizes seem to show a similar parabolic behavior independent of the blockiness of particles. Following the research of Janda *et al.*[18], the profiles are rescaled by the velocity at the exit center (v_c), and the horizontal position is rescaled by R. It is observed that the rescaled profiles are superimposed in all cases as shown in Figs. 6(a′)–6(f′). For all cases, the normalized vertical velocity profiles can be appropriately fitted by

$$v(x) = v_c\left(1-(x/R)^2\right)^{1/2}, \tag{13}$$

and thus share the uniform self-similar law. The fitting results are consistent with the experimental results for disks,[18] which conform with the free fall arch hypothesis.

The central vertical velocity v_c as a function of outlet size is shown in Fig. 7. As observed in Ref. [40], the fitting by square root law ($v_c = \sqrt{2\gamma g R}$) suggested in Ref. [18] is not completely satisfactory. We adjust the velocity in the center of outlet by

$$v_c = \gamma_v\sqrt{2gR}\left[1-\alpha\exp\left[-\beta R\right]\right], \tag{14}$$

with the same parameters α and β as those obtained for the packing fraction profiles in Eq. (12). The other fitting parameters are $\gamma_v = 1.48$, $\gamma_v = 1.46$, $\gamma_v = 1.41$, $\gamma_v = 1.40$, $\gamma_v = 1.39$, and $\gamma_v = 1.37$ for particles with blockiness $n = 2$, $n = 4$, $n = 6$, $n = 8$, $n = 10$, and $n = 12$, respectively, v_c is found to decrease monotonically with blockiness increasing, whereas the effect of n on v_c is very marginal when $n \geq 8$ due to the variation in particle shape is fairly subtle. Given that the height of the free fall arch relates to v_c,[18] this implies that the height of the free fall arch depends on the blockiness of superelliptical particles. The same fitting parameters in $1-\alpha e^{-\beta R}$ suggest that there may be a common mechanism for the decrease in packing fraction and velocity in the outlet center as the outlet size decreases.[40]

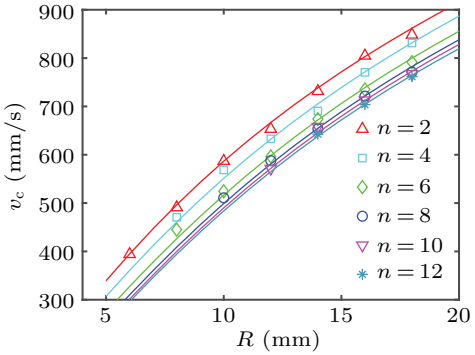


Fig. 7. Plots of velocity in the outlet center (v_c) *versus* R.

3.3. Coarse-grained fields of packing fraction and velocity

To further study the flow behaviors varying with the blockiness of particles, we compute the packing fraction and

vertical velocity fields during steady flow by using coarse-graining technique[19,20] based on the simulation data. Considering the anisotropic nature of superelliptical particles, the form of the 2D circular Gaussian coarse-graining function is modified into a superelliptical Gaussian function, which is expressed as

$$f(x,y) = \frac{1}{S}\exp\left[-\frac{x^n}{2a^n} - \frac{y^n}{2b^n}\right]$$

in the body-fixed coordinate system (x–y), where a and b are chosen to be the major and minor axis of the particle, and S is such a normalization constant that the integral over the coarse-graining function is unity. We can obtain $f(X,Y)$ in space fixed system (X–Y) by transformation $x = (Y - Y_C)\sin\theta + (X - X_C)\cos\theta$ and $y = (Y - Y_C)\cos\theta - (X - X_C)\sin\theta$, in which (X_C, Y_C) is the particle's centroid. For example, the superelliptical coarse-graining function corresponding to a particle ($n = 6$) that is tilted 70° with respect to X axis is shown in Fig. 8.

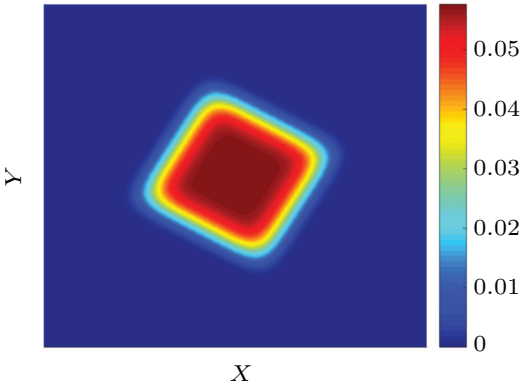


Fig. 8. Superelliptical coarse-graining function, tilted 70° with respect to X axis.

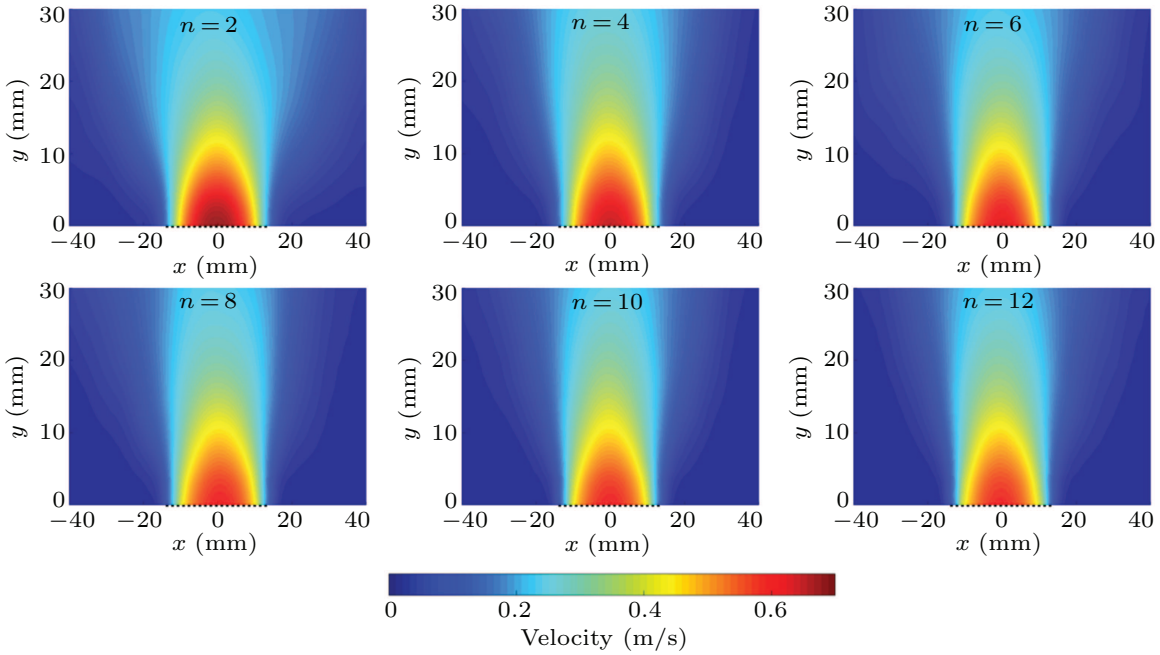


Fig. 9. Vertical velocity fields for particles with different blockinesses as indicated above each panel. The color bar is the same for all plots. In all cases, $D = 28$ mm, as indicated by the dotted line.

The spatial velocity fields for different particle systems at the outlet size of $R = 14$ mm are presented in Fig. 9. We can distinguish some major features of the flow zones from these maps. In discharge process, a stagnant zone with relatively high density and almost vanishing velocity is formed near the side and bottom walls, and the granular flow is funnel-shaped. The stagnant zone seems to gradually enlarge with blockiness increasing. The core flow zone can be clearly seen right above the orifice, where the particle velocity is very large compared with that outside the core. It is shown that the velocity field becomes weaker with the increase of particle blockiness in the core flow region, indicating that particles with larger blockiness have a lower downstream velocity, which results in the lower flow rate of particles with larger blockiness.

Now we turn to studying the volume fraction maps (Fig. 10). Overall, it can be noted that the density is considerably higher on either side of the outlet than in the central part of the silo above the orifice. There are two roughly triangular areas of low packing fractions (blue on the map) near and inside the outlet edges in the central region of the map, which become more pronounced with blockiness increasing. This indicates that the packing fraction decreases to a certain minimum near the limit of the orifice and then starts to increase, and the minimum packing fraction decreases as particle blockiness increases. To verify this behavior, figure 11 presents the horizontal packing fraction profiles in the region just above the orifice ($D = 28$ mm), which are calculated by using the same method as in Fig. 4. It can be seen that all packing fractions show an upward trend near the exit edge, with the minimum

fraction decreasing with particle blockiness, which is compatible with the packing fraction fields in the same region. The vertical lines indicate the location of the two roughly triangular areas in Fig. 10.

This indicates that a lower density near the outlet is required to maintain continuous flow for particles with larger blockiness, which is due to the stronger face-to-face contacts among more square particles. In addition, for particle systems with larger blockiness, some yellowish lines can be discerned, which may correspond to shear bands.

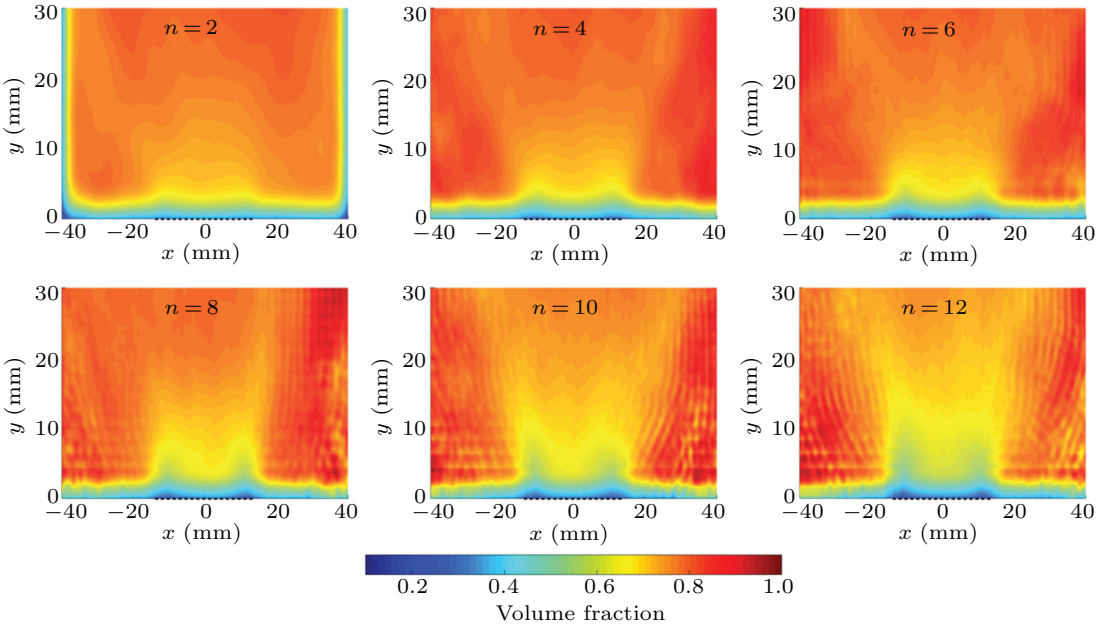


Fig. 10. Packing fraction fields for particles with different blockinesses. In all cases, $D = 28$ mm, as indicated by the dotted lines.

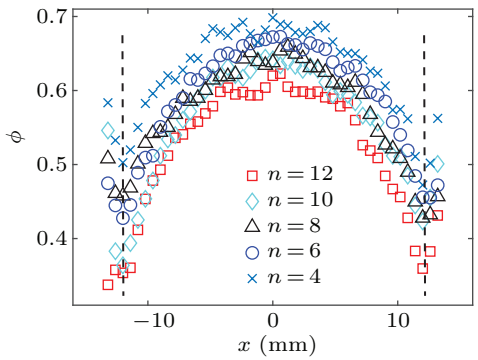


Fig. 11. Horizontal packing fraction profiles for particles with different blockinesses in the region just above the orifice. In all cases, $D = 28$ mm.

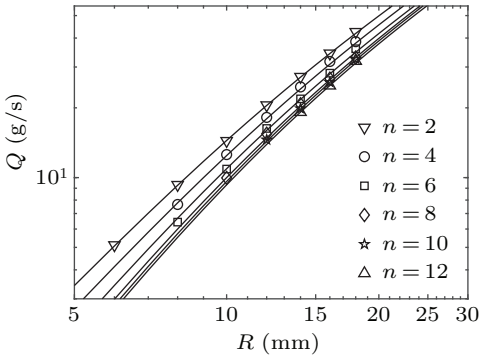


Fig. 12. Plots of mass flow rate *versus* R for particles with different blockinesses, with symbols representing simulated data and the lines corresponding to the results from Eq. (15).

3.4. Calculation of flow rate

Assuming that the volume and velocity profiles during discharge are stationary, the mass flow rate (Q) is calculated from

$$Q = \int_{-R}^{R} \sigma\phi(x)v(x)\,\mathrm{d}x,$$

in which σ is the surface density since, for we are considering the problem under 2D situation.

Combining Eqs. (11)–(14), the flow rate can be expressed as

$$Q = 2\sigma\gamma_v\phi_\infty\sqrt{2gR}\left[1-\alpha\exp\left(-\beta R\right)\right]^2 \times \int_0^R \left(1-\left(\frac{x}{R}\right)^2\right)^{1/2+v_\phi}\mathrm{d}x.$$

After solving the integral and incorporating the obtained parameters, the discharge mass flow rate from a 2D silo is then

$$Q = C'\sigma\gamma_v\phi_\infty\sqrt{g}R^{3/2}\left[1-\alpha\exp\left(-\beta R\right)\right]^2, \qquad (15)$$

where $C' = \sqrt{2}\mathrm{B}(1/2, 3/2+v_\phi)$, with $\mathrm{B}(1/2, 3/2+v_\phi)$ being the Beta function. The parameters in Eq. (15) can be explained from the self-similar packing fraction and velocity profile at the outlet. By contrast, the physical meaning of the fitting parameter k introduced in Eq. (1) is subtle. The comparison between simulated results and the prediction of Eq. (15) is presented in Fig. 12, revealing that they are in good agreement with each other. As indicated in Refs. [18,40], the information about profiles of the packing fraction and velocity of particles near the outlet allows us to make a reliable prediction of

the flow rate, based on physical observations. As discussed in Subsection 3.2, the physical parameters that govern the exit profiles of packing fraction and velocity depend on the particle blockiness parameter as shown in Fig. 13. However, further studies are needed to verify the exact relationship between them. Hence, once the correlation between the physical parameters in Eq. (15) and the particle blockiness is elucidated, it is likely to estimate the flow rate of superelliptical particles for various outlet sizes.

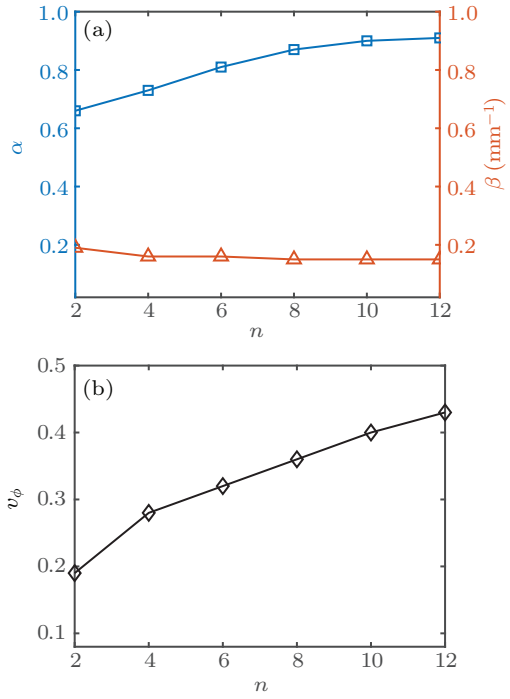


Fig. 13. Plots of (a) α and β, and (b) v_ϕ *versus* particle blockiness (n).

4. Summary and conclusions

The discharge flow of superelliptical particles from a 2D silo is investigated by using DEM. The flow rate for particles of various blockiness in the stationary regime is obtained, which decreases monotonically with blockiness increasing. The time-averaged packing fraction and velocity profiles at the outlet for particles with various blockiness are systematically measured and analyzed.

In all cases, the packing fraction profiles exhibit self-similar features that can be suitably adjusted by using fractional power functions with dimensionless orifice size. The fitting parameters are shown to be dependent on particle blockiness, implying that the particle shape has an effect on the spatial distribution of packing fraction near the orifice. The central packing fraction at the outlet displays an asymptotic growth and can be fitted with an exponential saturation. In all cases, the velocity profiles obey the definite self-similar law that is compatible with the experimental results,[18] conforming with the free fall arch hypothesis. The velocity of particles at the center of outlet is shown to decrease as blockiness increases, implying that the height of free fall arch may vary with blockiness. It is observed that larger particle blockiness will lead to lower velocity and packing fraction at an identical outlet, which results in a lower flow rate for particles with larger blockiness. For all cases, the flow rates are calculated from the packing fractions and velocity profiles and agree well with the simulated data.

The results show that the shape of particle affects packing fraction and kinematics of particles in the discharge flow from a silo. The flow rate of the superelliptical particles can be theoretically predicted if the general correlation between the physical parameters that govern the packing fraction and velocity profiles and the blockiness of particle is clarified. To this end, investigations are needed to confirm and extend the present results.

Acknowledgement

Project supported by the Science and Technology Program of Guizhou Province, China (Grant No. [2018]1048).

References

[1] Aranson I S and Tsimring L S 2006 *Rev. Mod. Phys.* **78** 641
[2] Bursik M, Patra A, Pitman E B, Nichita C, Macias J L, Saucedo R and Girina O 2005 *Reports Prog. Phys.* **68** 271
[3] Zuriguel I, Parisi D R, Hidalgo R C, Lozano C, Janda A, Gago P A, Peralta J P, Ferrer L M, Pugnaloni L A, Clément E, Maza D, Pagonabarraga I and Garcimartín A 2014 *Sci. Rep.* **4** 7324
[4] Denisov D V, Lörincz K A, Uhl J T, Dahmen K A and Schall P 2016 *Nat. Commun.* **7** 10641
[5] Cleary P W, Hilton J E and Sinnott M D 2017 *Powder Technol.* **314** 232
[6] Zhu H P, Zhou Z Y, Yang R Y and Yu A B 2008 *Chem. Eng. Sci.* **63** 5728
[7] Zhong W, Yu A, Liu X, Tong Z and Zhang H 2016 *Powder Technol.* **302** 108
[8] Govender N, Wilke D N, Wu C Y, Khinast J, Pizette P and Xu W 2018 *Chem. Eng. Sci.* **188** 34
[9] Seville J, Tüzün U and Clift R 1997 *Processing of Particulate Solids* (London: Blackie Academic & Professional)
[10] Beverloo W A, Leniger H A and van de Velde J 1961 *Chem. Eng. Sci.* **15** 260
[11] Ristow G H 1997 *Physica A* **235** 319
[12] Zhu H W, Wang L P, Shi Q F, Li L S and Zheng N 2019 *Powder Technol.* **345** 676
[13] Aguirre M A, Grande J G, Calvo A, Pugnaloni L A and Géminard J C 2010 *Phys. Rev. Lett.* **104** 238002
[14] Hilton J E and Cleary P W 2011 *Phys. Rev. E* **84** 11307
[15] Lin P, Zhang S, Qi J, Xing Y M and Yang L 2015 *Physica A* **417** 29
[16] Tang J and Behringer R P 2016 *Europhys. Lett.* **114** 34002
[17] Wang T, Li X, Wu Q, Jiao T, Liu X, Sun M, Hu F and Huang D 2018 *Chin. Phys. B* **27** 124704
[18] Janda A, Zuriguel I and Maza D 2012 *Phys. Rev. Lett.* **108** 248001
[19] Rubio-Largo S M, Janda A, Maza D, Zuriguel I and Hidalgo R C 2015 *Phys. Rev. Lett.* **114** 238002
[20] Weinhart T, Labra C, Luding S and Ooi J Y 2016 *Powder Technol.* **293** 138
[21] Cleary P W and Sawley M L 2002 *Appl. Math. Model.* **26** 89
[22] Li J, Langston P A, Webb C and Dyakowski T 2004 *Chem. Eng. Sci.* **59** 5917
[23] Langston P A, Al-Awamleh M A, Fraige F Y and Asmar B N 2004 *Chem. Eng. Sci.* **59** 425
[24] Kanzaki T, Acevedo M, Zuriguel I, Pagonabarraga I, Maza D and Hidalgo R C 2011 *Eur. Phys. J. E* **34** 133
[25] Liu S D, Zhou Z Y, Zou R P, Pinson D and Yu A B 2014 *Powder Technol.* **253** 70

[26] Ashour A, Wegner S, Trittel T, Börzsönyi T and Stannarius R 2017 *Soft Matter* **13** 402
[27] Börzsönyi T, Somfai E, Szabó B, Wegner S, Mier P, Rose G and Stannarius R 2016 *New J. Phys.* **18** 93017
[28] Tao H, Jin B and Zhong W 2011 *2011 International Conference on Electric Technology and Civil Engineer,* April 22–24, 2011 Lushan, China, p. 678
[29] Höhner D, Wirtz S and Scherer V 2013 *Powder Technol.* **235** 614
[30] Höhner D, Wirtz S and Scherer V 2015 *Powder Technol.* **278** 286
[31] Han Y, Jia F, Li G, Liu H, Li J and Chen P 2019 *Adv. Powder Technol.* **30** 1870
[32] Wang S, Zhuravkov M and Ji S 2020 *Soft Matter* **16** 7760
[33] Hafez A, Liu Q, Finkbeiner T, Alouhali R A, Moellendick T E and Santamarina J C 2021 *Sci. Rep.* **11** 3309
[34] Zhang Z, Liu Y, Zheng B, Sun P and Li R 2022 *Arab. J. Sci. Eng.* **47** 5721
[35] Ni R, Gantapara A P, De Graaf J, Van Roij R and Dijkstra M 2012 *Soft Matter* **8** 8826
[36] Zhao C, Cheng X, Peng Y and Li C 2020 *Powder Technol.* **375** 369
[37] Zhao C, Gao Q, Chen Y and Li C 2021 *Powder Technol.* **387** 481
[38] Chen X, Peng Y, Li C and Zhao C 2022 *Powder Technol.* **407** 117657
[39] Nedderman R M, Tüzün U, Savage S B and Houlsby G T 1982 *Chem. Eng. Sci.* **37** 1597
[40] Zhou Y, Ruyer P and Aussillous P 2015 *Phys. Rev. E* **92** 062204